Supplement of The Cryosphere, 17, 407–425, 2023
https://doi.org/10.5194/tc-17-407-2023-supplement

The Cryosphere
Open Access

Supplement of

Modulation of the seasonal cycle of the Antarctic sea ice extent by sea ice processes and feedbacks with the ocean and the atmosphere

Hugues Goosse et al.

Correspondence to: Hugues Goosse (hugues.goosse@uclouvain.be)

Supplementary discussion: temperature response in ThickIce and ThinIce experiments

In ThickIce, a cooling is observed in summer and in regions in winter close to the ice edge compared to the reference experiment (Fig. S5) due to the larger sea ice extent. However, this does not overwhelm the effect of the larger winter sea ice formation (Fig. 4) and thus the larger heat fluxes to the atmosphere within the pack that leads to an air temperature increase that dominates the regional mean (Fig. 8).

The opposite should occur in the ThinIce experiments. The lower sea ice formation (Fig. 4) and oceanic heat losses in ThinIce should lead to a cooling of the atmosphere within the ice pack, while the smaller ice extent should be associated with an atmospheric warming in the regions that are ice free in ThinIce and ice covered in the reference experiment. However, we find that the atmospheric warming due to a reduced ice extent expands to most of the pack in ThinIce, even in winter with cooling restricted to some regions close to the continent (Fig. S5). This extended warming is likely due to the strong changes in albedo and absorbed solar radiation in ThinIce (Fig. S4). The dominant role of the albedo is consistent with the generally colder temperatures in the first winter of ThinIce_PARA_Mar (Fig. 8), when the albedo effect did not yet have the time to act given that the experiments start at the end of summer. The larger fraction of leads within the ice pack also contributes to the warming in ThinIce.

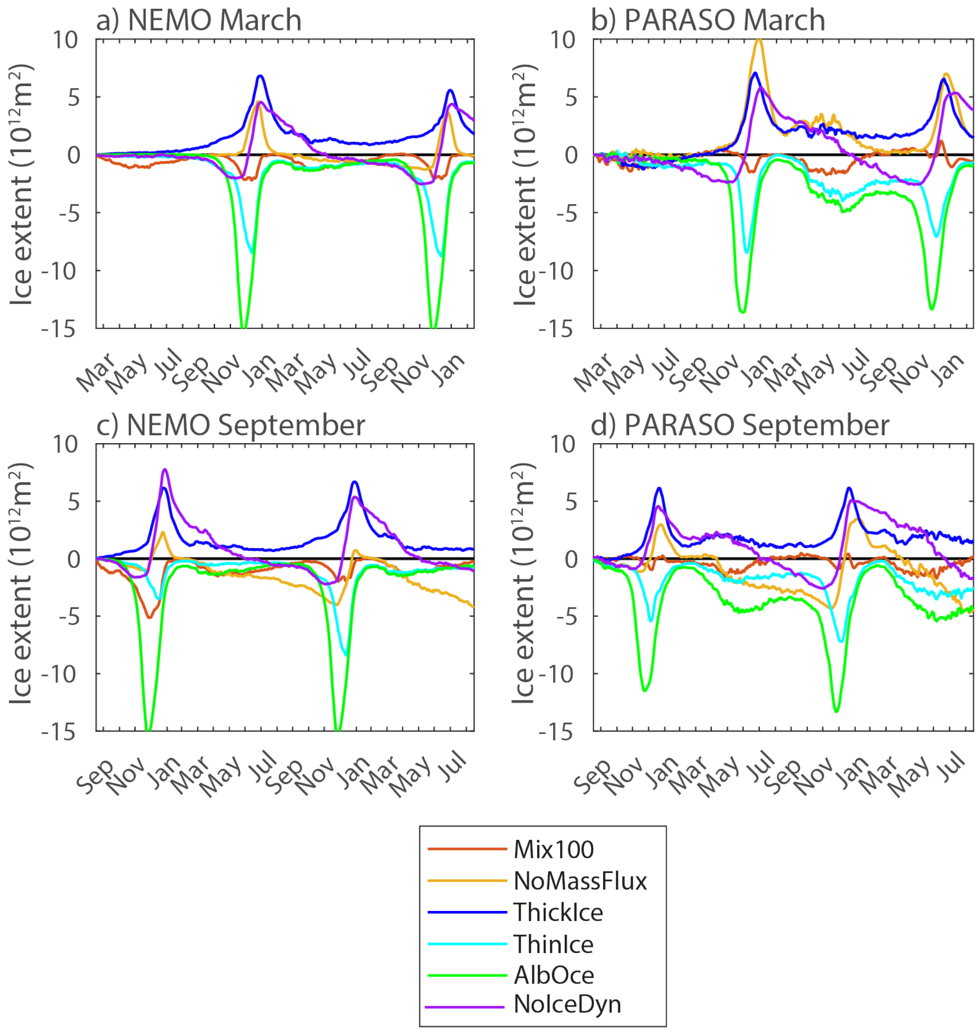

Figure S1. Anomaly of Antarctic sea ice extent (in 10^{12} m^2) compared to the corresponding reference simulation in the group of experiments starting in March (top row) and September (bottom) for the NEMO (left column) and PARASO configurations (right column).

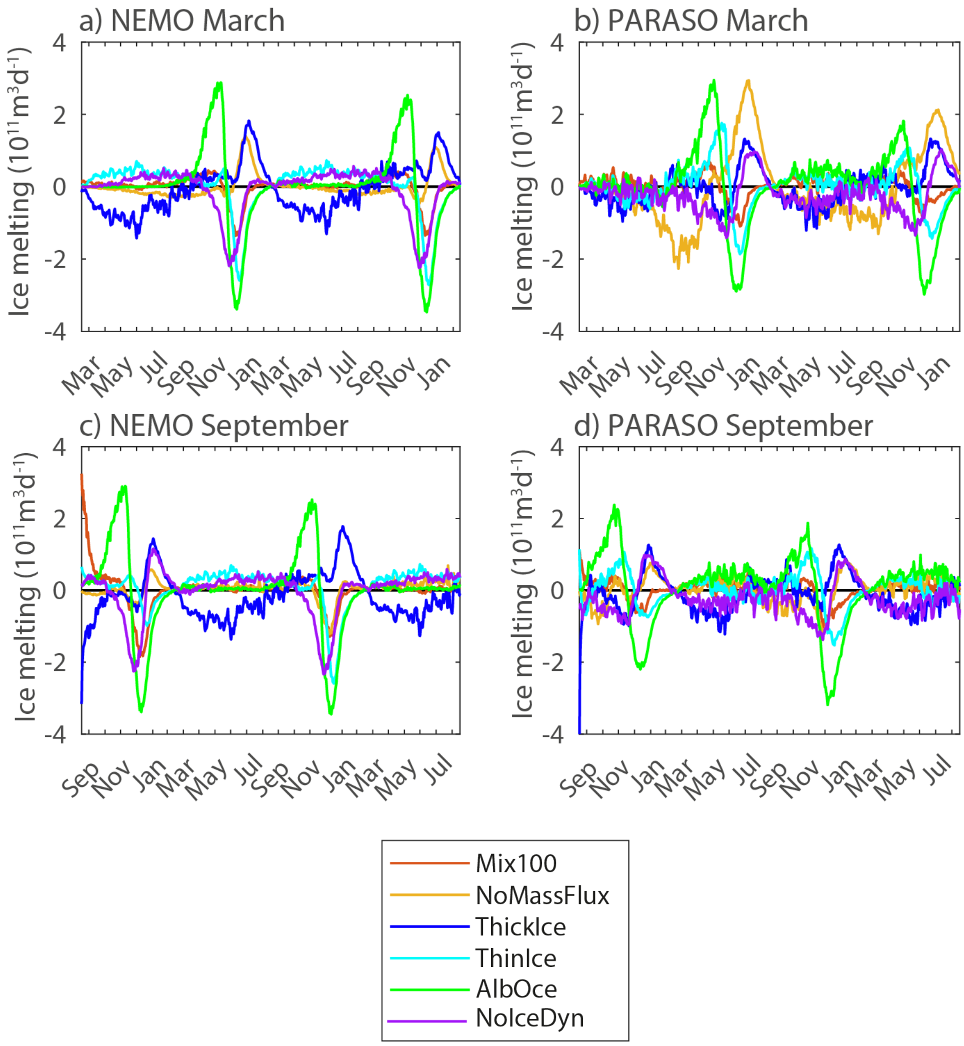

Figure S2. Anomaly of mass flux due to sea ice growth and melt (counted positive for melting) integrated over the Southern Ocean (in 10^{11} m^{3}d^{-1}) compared to the corresponding reference simulation in the group of experiments starting in March (top row) and September (bottom) for the NEMO (left column) and PARASO configurations (right column).

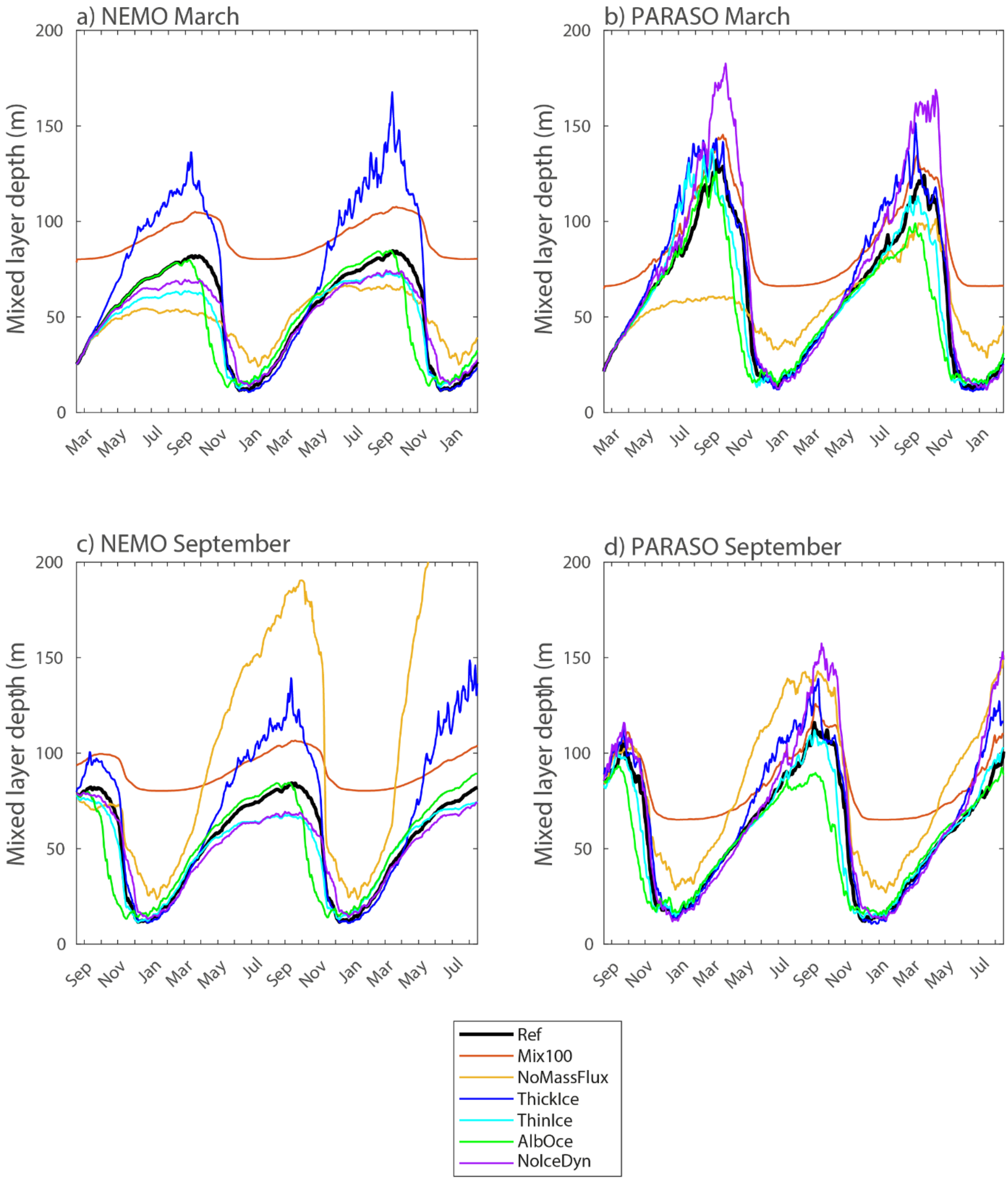

Figure S3. Mixed layer depth (in m) averaged over the ocean region south of 60°S in the group of experiments starting in March (top row) and September (bottom) for the NEMO (left column) and PARASO configurations (right column).

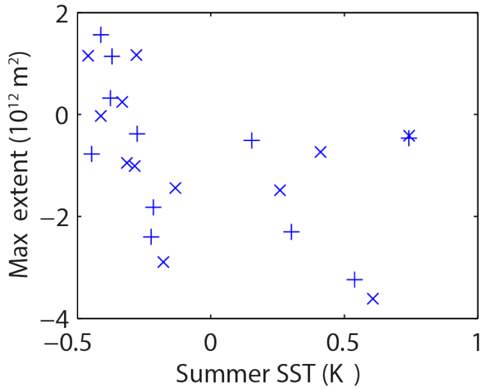

Figure S4. Maximum sea ice extent anomaly (in $10^{12}m^2$) compared to the reference experiment as a function of the sea surface anomaly averaged over the region south of 60°S (in K) in the previous summer for the second year in the experiments starting in March and for the first minimum and second maximum for the experiments starting in September.

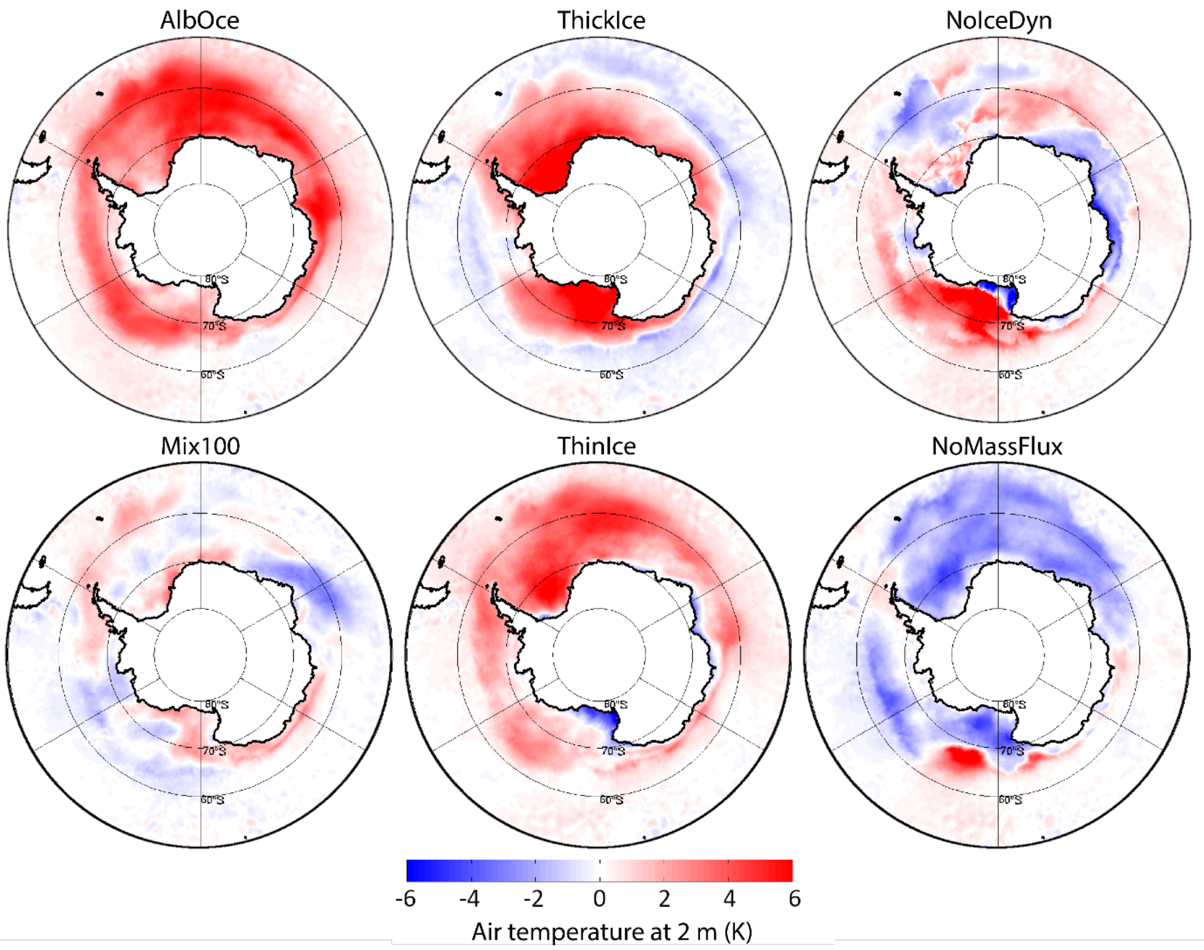

Figure S5. Difference in surface air temperature (in K) between the PARASO experiment in winter (July-August-September) of the second year of the experiment starting in March and the corresponding reference experiment.

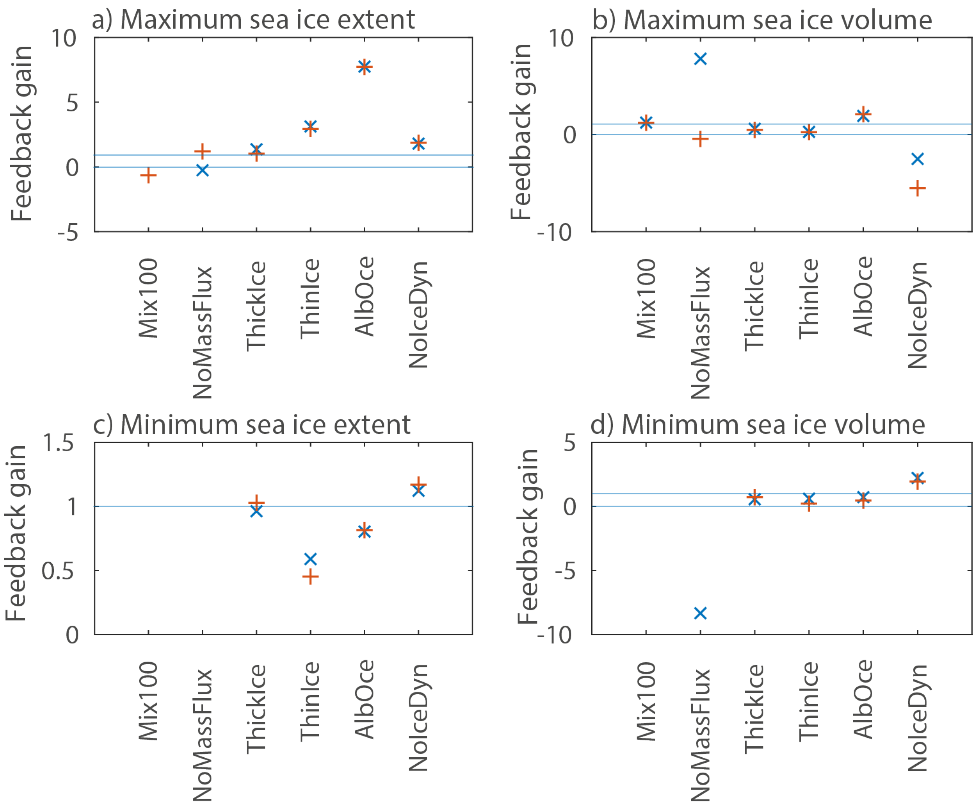

Figure S6. Feedback gain for experiments starting in March (blue x) and September (red +) for the a) maximum sea ice extent, b) maximum sea ice volume, c) minimum sea ice extent and d) minimum sea ice volume. We have not displayed the feedback gain when the uncoupled response is smaller than 0.2 million km^2 for sea ice extent or 0.2 thousand km^3 for sea ice volume to avoid large numbers of the feedback gains, as this value is used in the denominator of *G*. Light blue lines are drawn at values of 0 and 1.

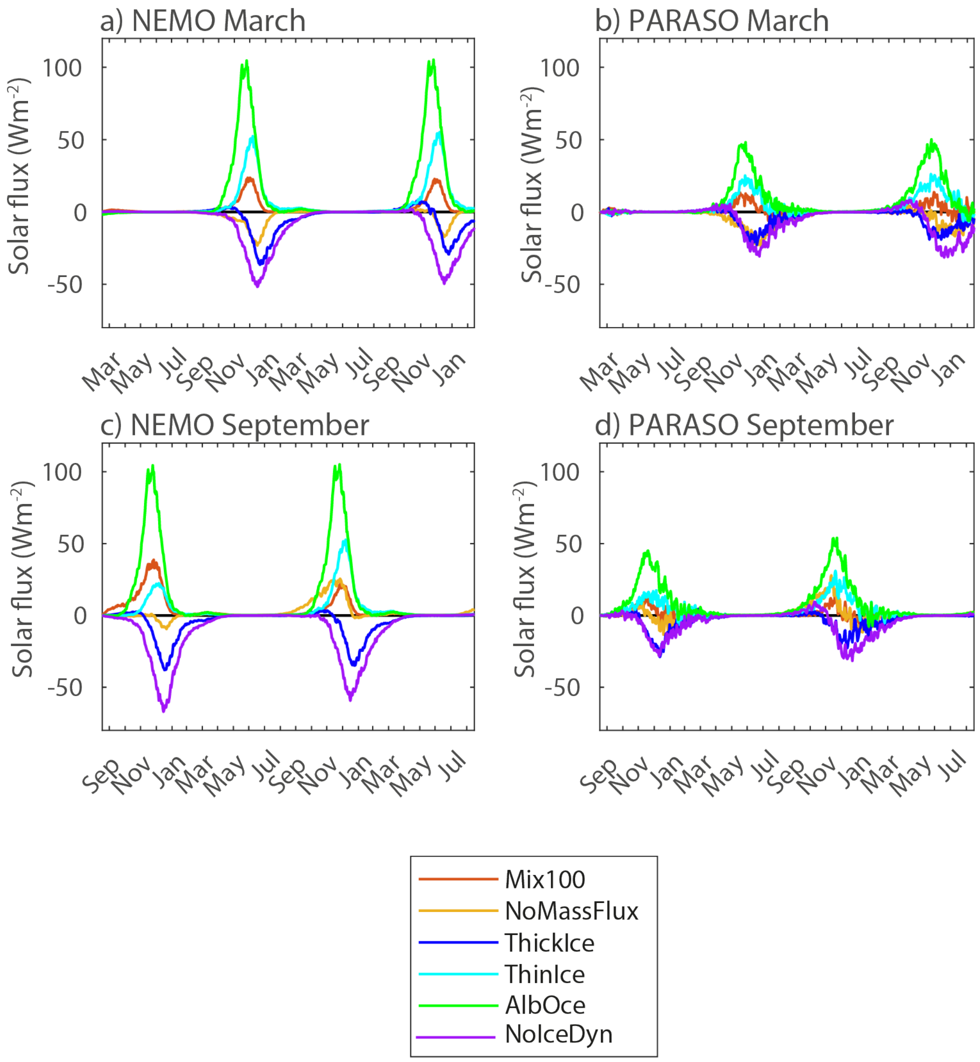

Figure S7. Anomaly of net solar radiation at the top of the ocean (in W m^{-2}) averaged over the ocean region south of 60°S compared to the corresponding reference simulation in the group of experiments starting in March (top row) and September (bottom) for the NEMO (left column) and PARASO configurations (right column).

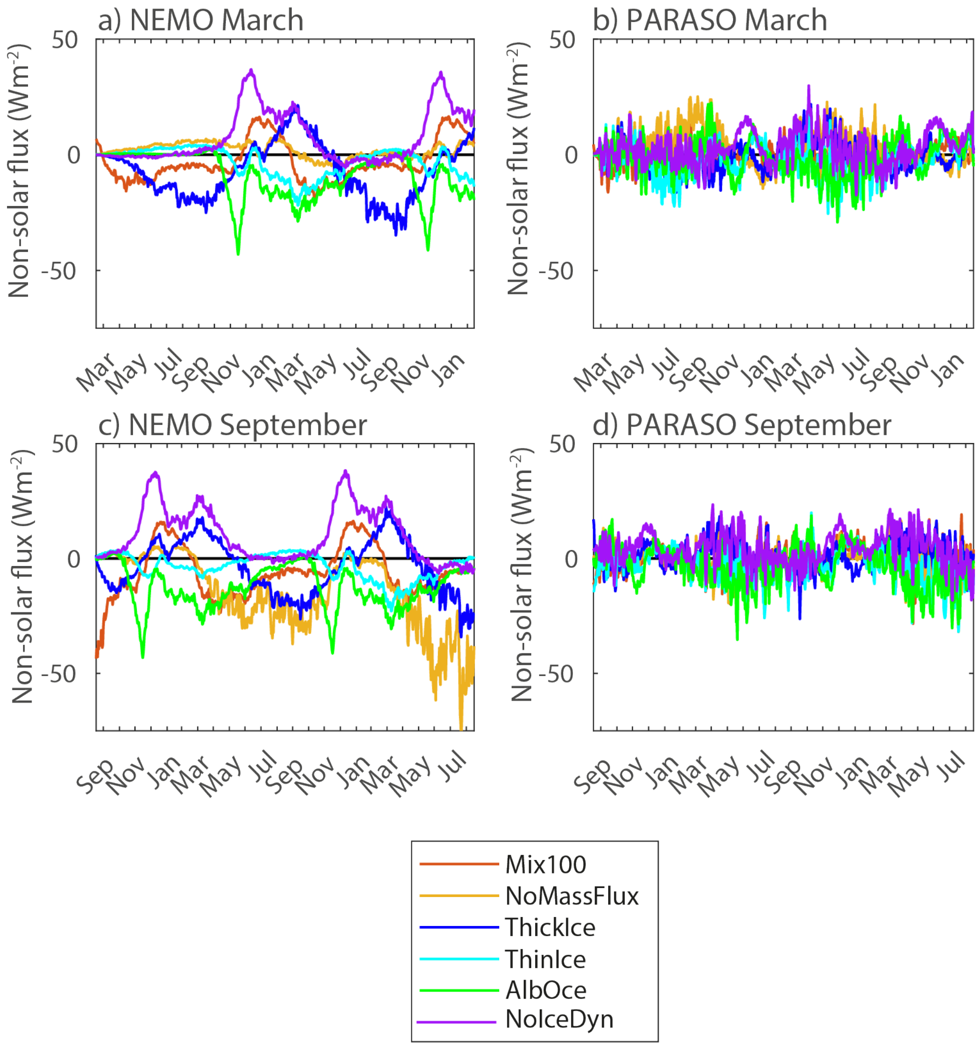

Figure S8. Anomaly of net non-Solar heat flux at the top of the ocean (in W m^{-2}) averaged over the ocean region south of 60°S compared to the corresponding reference simulation in the group of experiments starting in March (top row) and September (bottom) for the NEMO (left column) and PARASO configurations (right column).

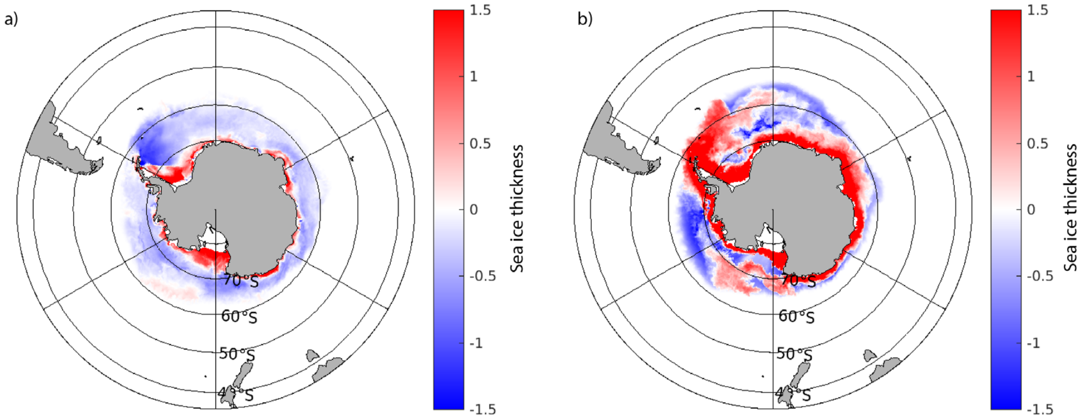

Figure S9. Difference in sea ice thickness (in m) in September of the second year between NoIceDYN_NEMO_Mar (left) and NoIceDYN_PARA_Mar (right) and the corresponding reference experiments.

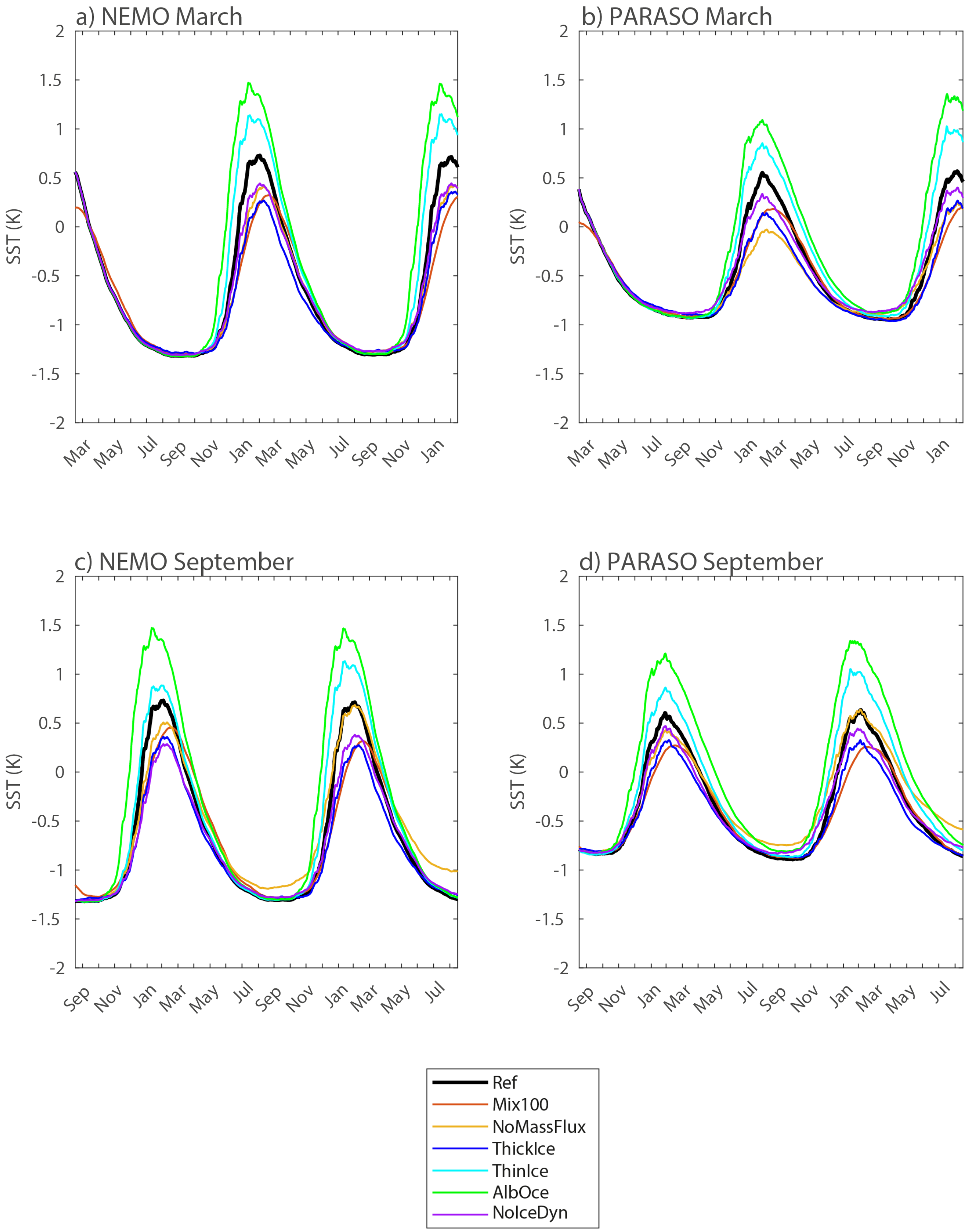

Figure S10. Sea surface temperature (in K) averaged over the ocean region south of 60°S in the group of experiments starting in March (top row) and September (bottom) for the NEMO (left column) and PARASO configurations (right column).